Ocean Engineering 289 (2023) 116287

Contents lists available at ScienceDirect

Ocean Engineering

journal homepage: www.elsevier.com/locate/oceaneng

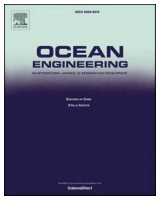

# A two-dimensional inverse crack tip element for shape sensing and structural health monitoring

Mingyang Li [a,b], Erkan Oterkus [b,*], Selda Oterkus [b]

[a] Ocean College, Jiangsu University of Science and Technology, Zhenjiang, China
[b] Department of Naval Architecture, Ocean and Marine Engineering, University of Strathclyde, Glasgow, United Kingdom

ARTICLE INFO

Handling Editor: Prof. A.I. Incecik

*Keywords:*
iFEM
Crack tip
Shape sensing
Structural health monitoring
Two-dimensional

ABSTRACT

inverse Finite Element Method (iFEM) is a powerful tool for shape sensing and structural health monitoring of marine structures and has several advantages with respect to some other existing approaches. However, current iFEM formulation is not suitable for marine structures having pre-existing cracks due to stress singularities at the crack tip. In this study, a two-dimensional inverse crack tip element formulation is presented. The element is suitable for thin structures under in-plane loading conditions. The inverse crack tip element allows determination of Stress Intensity factor values at the crack tip. To validate the accuracy and demonstrate the capability of the inverse crack tip element, six different numerical cases are considered for different geometry, loading and boundary conditions. iFEM analysis results are compared with regular finite element analysis results as the reference solution and very good agreement is observed between the two solutions demonstrating the capability of the current iFEM approach.

## 1. Introduction

Marine structures are subjected to harsh environmental conditions which can cause catastrophic consequences, financial loses, and environmental pollution. In order to ensure safety of marine structures, shape sensing and structural health monitoring (SHM) are effective approaches to be utilised by utilising sensor systems, collecting sensor data, processing the data, and finally making decisions.

According to Gherlone et al. (2012), a good SHM system should easily treat complicated structures and their boundary conditions. Moreover, the loading conditions, material properties, and even some inherent errors (which cannot be avoided during the process of measuring data) should not affect the stability and accuracy of the system. In addition, the SHM system must be fast enough to perform a real-time monitoring process (Gherlone et al., 2012). With the help of the SHM system, unusual behaviors, such as unhealthy conditions and structural failure, of the structure can be accurately detected. Furthermore, additional management including inspection, maintenance, and repair of the structure can also be enhanced under the guidance of SHM systems (Lu et al., 2009). The process of maintenance can be scheduled in a more orderly manner, which will reduce unnecessary inspection and repair. SHM has been used in many different applications such as aerospace (Di Sante, 2015), composites (Kinet et al., 2014), rail systems (Chen et al., 2020), bridges (Kromanis and Kripakaran, 2016), batteries (Xiong et al., 2018), etc.

There are various shape sensing approaches available in the literature. Amongst these Ko's Displacement Theory (Ko et al., 2007) is suitable for beam type structures. On the other hand, Model Method (Bang et al., 2012) can make predictions without material information and it is suitable for both beam and plate type structures. Another promising approach for shape sensing is inverse Finite Element Method (iFEM) developed by Tessler and Spangler (2003). iFEM is based on discretisation of the solution domain by using suitable inverse elements (beam, plate, shell or solid) and utilising collected strain data from sensors located on the structure. It is also robust and can be used for real-time monitoring for complex shapes. Moreover, there is no need to measure loading during the monitoring process.

There has been a significant progress throughout the years on iFEM methodology. Various different types of inverse elements have been developed for different types of structures. For instance, Tessler and Spangler (2004) developed a three-node inverse shell element (iMIN3) which is based on variation of in-plane displacements and bending rotations linearly, and transverse displacements quadratically along with in-plane coordinates. Tessler et al. (2012) extended the capability of

* Corresponding author.
*E-mail address:* erkan.oterkus@strath.ac.uk (E. Oterkus).

https://doi.org/10.1016/j.oceaneng.2023.116287
Received 17 August 2023; Received in revised form 24 October 2023; Accepted 4 November 2023
Available online 15 November 2023

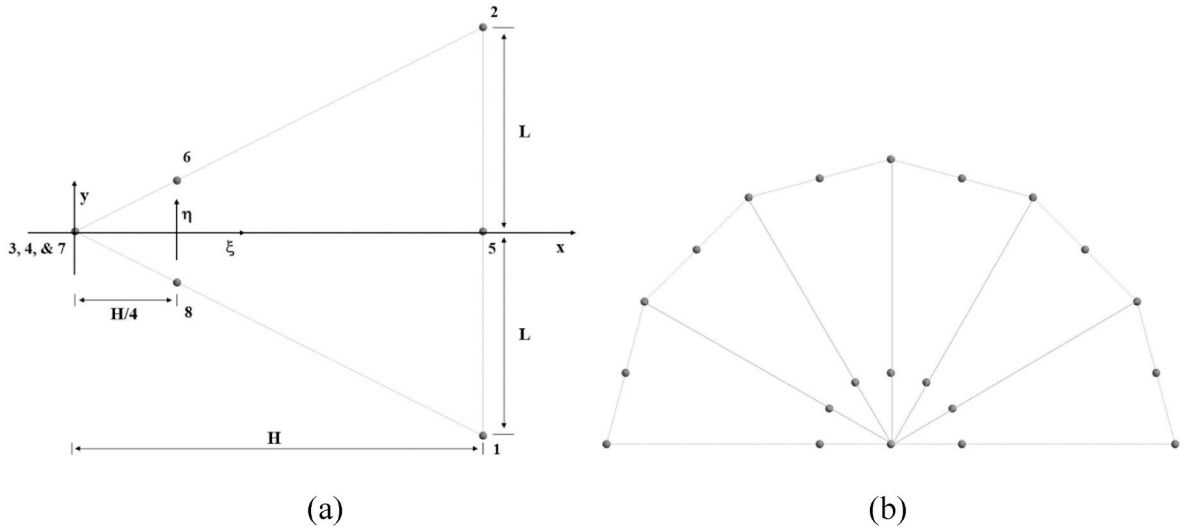


**Fig. 1.** (a) Quarter-point crack tip element and (b) quarter-point elements around the crack tip.

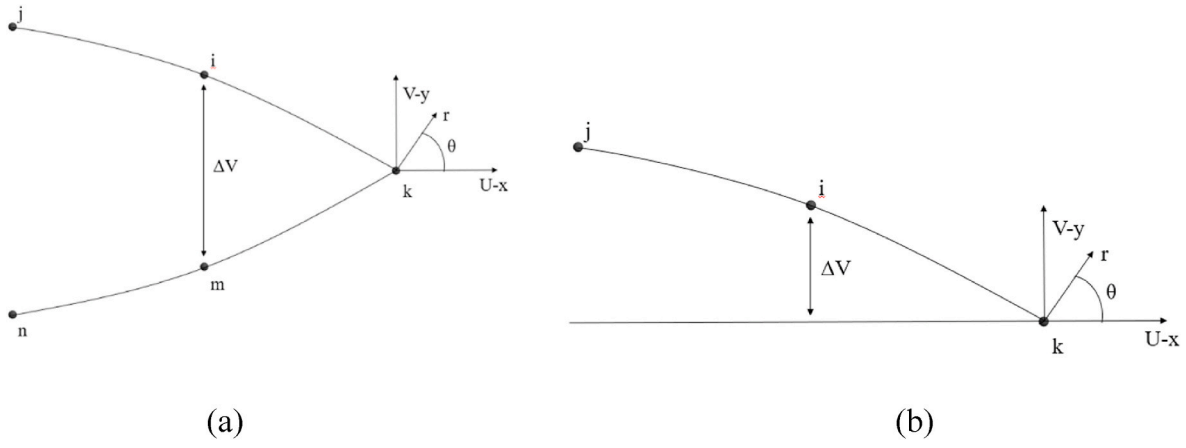


**Fig. 2.** The displacements of the crack tip for the displacement extrapolation method (a) full model, (b) half (symmetrical) model.

**Table 1**
Cases for estimating the SIF at the crack tip.

| | |
|---|---|
| Case 1 | Rectangular bar with two edge cracks |
| Case 2 | Rectangular bar with a central crack |
| Case 3 | Fine mesh for Case 1 for opening SIF case |
| Case 4 | Fine mesh for Case 2 for opening SIF case |
| Case 5 | In-plane shear SIF case |
| Case 6 | Mixed-mode SIF case |

iMIN3 element for large deformations. Gherlone et al. (2012) developed an inverse beam element based on Timoshenko beam formulation. Kefal et al. (2016) introduced a four node shell element with drilling degree-of-freedom (iQS4). This inverse element has been successfully utilised for monitoring of various marine structures (Kefal and Oterkus, 2015) including a chemical tanker (Kefal and Oterkus, 2016a), containership (Kefal and Oterkus, 2016b), bulk carrier (Kefal et al., 2018a), and offshore wind turbine (Li et al., 2023). By using First-order

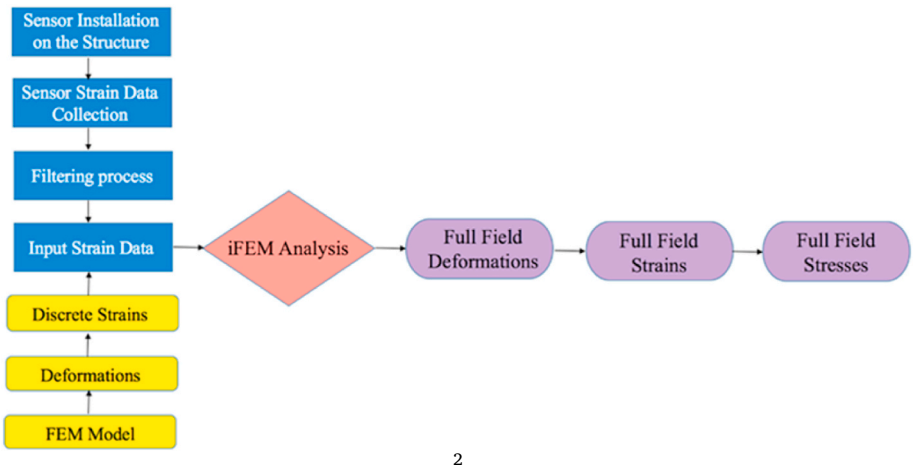


**Fig. 3.** Flow chart of the analysis process.

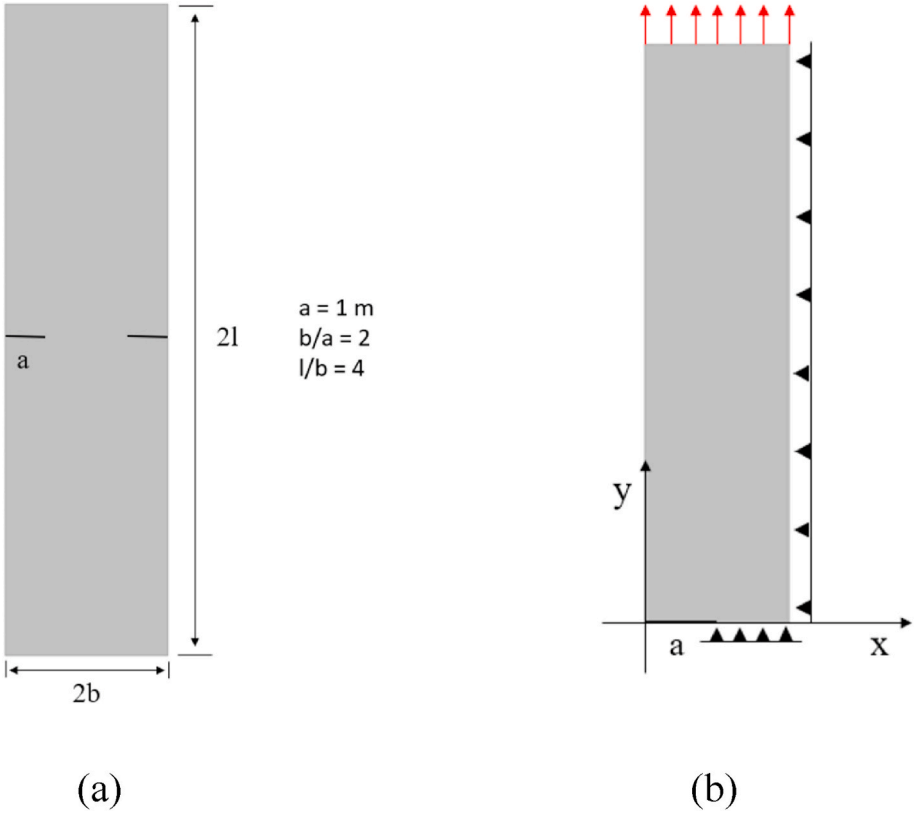


**Fig. 4.** (a) The geometry of the plate with two edge cracks and (b) the loading and symmetry boundary conditions of the quarter of the model for Case 1.

Deformation Theory, Kefal (2019) developed an eight node curved shell element (iCS8). In another study, de Mooij et al. (De Mooij et al., 2019) presented a novel inverse solid element formulation by considering various benchmark problems. iFEM has also been applied for composite materials. Cerracchio et al. (2015) and Kefal et al. (2018b) developed plate and shell elements suitable for composite and sandwich structures. iFEM has also been used for damage prediction in structures (Colombo et al., 2019). In order to reduce number of required sensors for iFEM analysis, Kefal and Oterkus (2020) introduced isogeometric iFEM analysis which was further explored in some other studies (Zhao and Bao, 2021; Zhao et al., 2020).

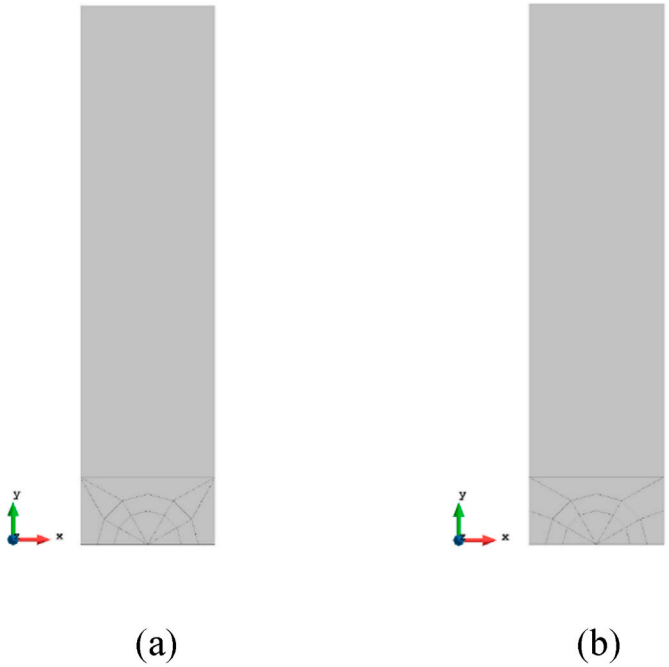


**Fig. 5.** The fine mesh for Case 1. (a) FEM, (b) iFEM.

Contrary to this progress on iFEM methodology, there is currently no inverse crack tip element available in the literature. The crack tip elements can achieve the requirement of singularity at the crack tip. Therefore, traditional iFEM elements cannot be applied to structures with pre-existing cracks. The development of the inverse plane crack tip element will fill this gap and extend the application range of iFEM. Additionally, with the generation of the inverse crack tip element, the SIF at the crack tip can also be monitored. With a given fracture criterion, the propagation of the crack can also be predicted.

Therefore, in this study, a two-dimensional inverse crack tip element formulation is presented. The element is suitable for thin structures under in-plane loading conditions. To validate the accuracy and demonstrate the capability of the inverse element, six different numerical cases are presented by considering different geometry, loading and boundary conditions. iFEM analysis results are compared with regular finite element analysis results as the reference solution.

## 2. Two-dimensional inverse crack tip element formulation

The inverse 8-node crack tip element is developed by applying the weighted-least-squares approach to the plane crack tip element formulation which was introduced by Barsoum, 1976, 1977. The crack tip

**Table 2**
The results for Case 1.

| Case 1 | | $U$ (m) | $V$ (m) | SIF- $K_I$ |
|---|---|---|---|---|
| (a) | FEM | 5.668E-03 | 4.329E-02 | 2.017E+09 |
| (b) | iFEM | 5.881E-03 | 4.371E-02 | 1.870E+09 |
| Differences between (a) and (b) | | 3.76% | 0.97% | 7.31% |

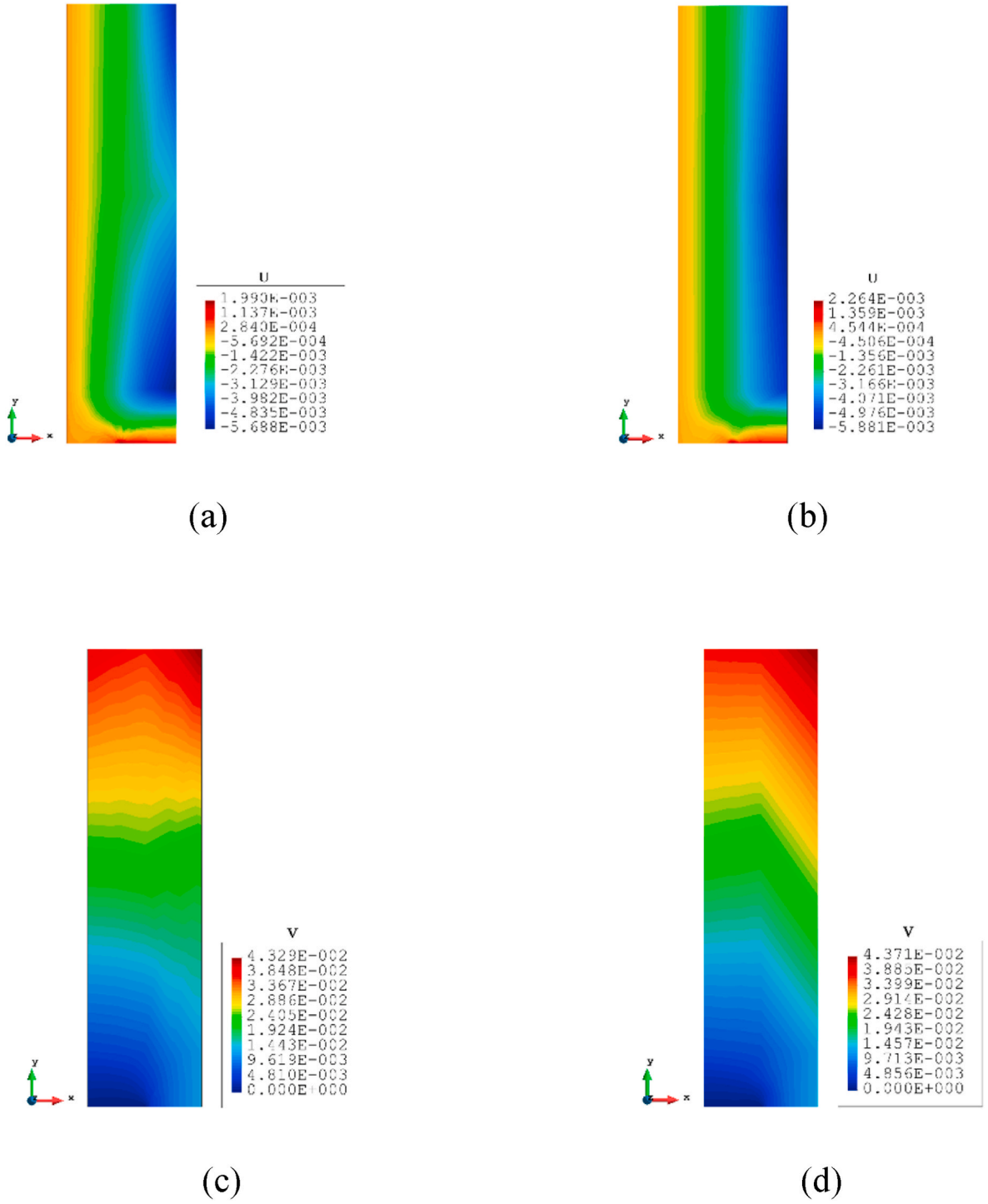


**Fig. 6.** The contour plots for Case 1. The displacements in x-direction, $U$: (a) FEM, (b) iFEM. The displacements in y-direction, $V$: (c) FEM, (d) iFEM.

element can capture singularity by shifting two mid-side nodes to the quarter of the line. Usually, the original quadrilateral element is degenerated into a kind of triangular element (see Fig. 1(a)). Nodes 3, 4, and 7 are transformed to overlap each other, and node 6 and node 8 are moved to the quarter of the line (Nikishkov, 2013). The length of the element is $H$ in the x-direction and the height is $2L$ (Fig. 1(a)), which means that node 6 and node 8 are located at $\left(\frac{H}{4}, \frac{L}{4}\right)$ and $\left(\frac{H}{4}, -\frac{L}{4}\right)$, respectively, in the local coordinate system. The parameters $H$ and $L$ can be calculated by the nodal distance. When defining the crack tip element, a transformation is required from the quadrilateral element in the normalized coordinate system to the degenerated triangular element in the local coordinate system. By doing so, it will contribute to another Jacobian matrix apart from the Jacobian which is used to link the shape functions between the global coordinate system and the normalized coordinate system. The Jacobian matrix can be obtained by the following relationship, according to the positional relation shown in Fig. 1(a) as

$$x = \frac{H(1-\eta)^2}{4} \tag{1a}$$

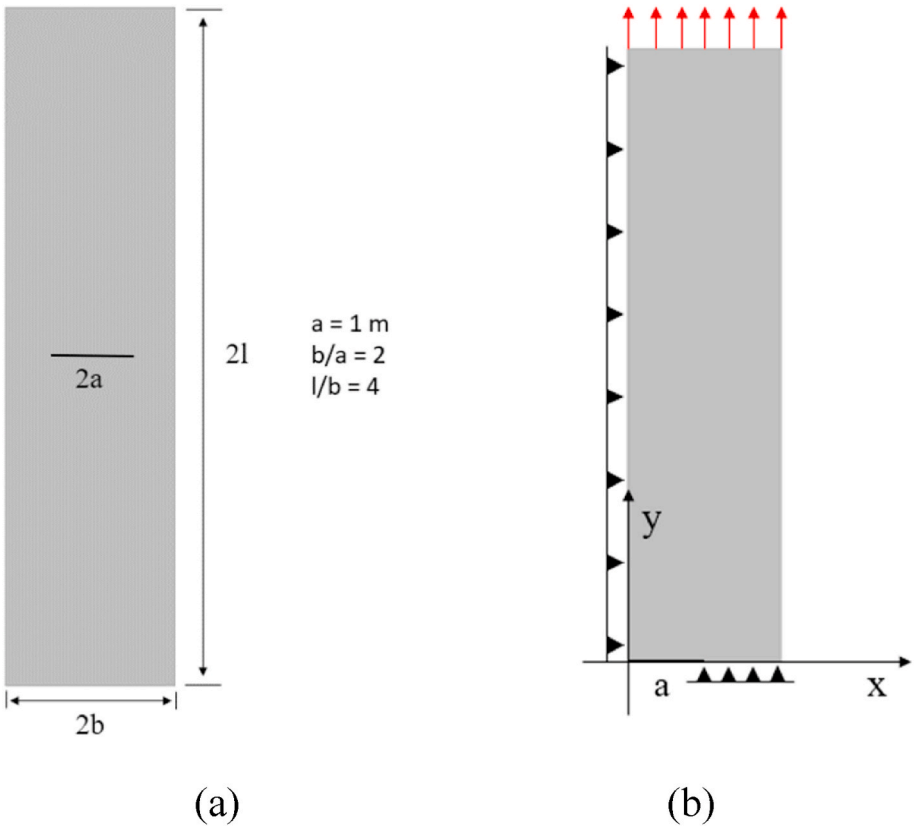


**Fig. 7.** (a) The geometry of the plate with central a crack and (b) the loading and symmetry boundary conditions of the quarter of the model for Case 2.

$$y = \frac{L(1-\eta)^2\xi}{4} \tag{1b}$$

By differentiating the $x$ and $y$ against $\xi$ and $\eta$, the following Jacobian matrix can be obtained:

$$[J] = \begin{bmatrix} \frac{\partial x}{\partial \xi} & \frac{\partial y}{\partial \xi} \\ \frac{\partial x}{\partial \eta} & \frac{\partial y}{\partial \eta} \end{bmatrix} = \begin{bmatrix} 0 & \frac{L(1-\eta)^2}{4} \\ \frac{(-1)H(1-\eta)}{2} & \frac{(-1)L(1-\eta)\xi}{2} \end{bmatrix} \tag{2}$$

Then the $[J]$ will be used in the process of generating the coefficient matrix. It should be mentioned that the order of the node is not fixed and the expressions of the $[J]$ should also be updated correspondingly.

For the plane inverse crack tip element, there are three membrane strains $\varepsilon_{xx}$, $\varepsilon_{yy}$, and $\gamma_{xy}$ that need to be taken into account. The differences between the analytical strains and the experimental strains which are collected from the geometric centre of the quadrilateral element can be expressed in the form of a functional as:

$$\varphi(\mathbf{u}^e) = w_e \left\| \begin{Bmatrix} w_{xx}\left(\varepsilon_{xx} - \varepsilon_{xx}^{input}\right) \\ w_{yy}\left(\varepsilon_{yy} - \varepsilon_{yy}^{input}\right) \\ w_{xy}\left(\gamma_{xy} - \gamma_{xy}^{input}\right) \end{Bmatrix} \right\|^2 \tag{3}$$

By differentiating the functional given in Eq. (3) with respect to the nodal displacements to minimize the difference between the analytical and experimental strains for every single element, the following equation can be evaluated:

$$\frac{\partial \varphi(\mathbf{u}^e)}{\partial \mathbf{u}^e} = \mathbf{k}^e\mathbf{u}^e - \mathbf{f}^e = 0 \tag{4}$$

where

$$\mathbf{k}^e = \iint_A w_e(\mathbf{B}^m)^T\mathbf{B}^m \det(J)dxdy \tag{5a}$$

$$\mathbf{f}^e = \iint_A w_e(\mathbf{B}^m)^T \begin{Bmatrix} \varepsilon_{xx}^{input} \\ \varepsilon_{yy}^{input} \\ \gamma_{xy}^{input} \end{Bmatrix} \det(J)dxdy \tag{5b}$$

where $\mathbf{u}^e$ is the elemental displacement vector and for each node, there are two DOFs, i.e. horizontal displacement, $U$, and vertical displacement, $V$. $w_e$ is the weighting constant that can be specified based on the existence of the experimental strain inputs. If the experimental data is available for an element, a value of 1 will be used. Otherwise, a relatively small value such as $10^{-3}$ or $10^{-4}$ can be selected. Additionally, another group of weighting coefficients ($w_{xx}$, $w_{yy}$, and $w_{xy}$) is introduced to balance the relationship among the three strains and usually, 1 will be used for all of the coefficients. $\mathbf{B}^m$ is the matrix generated by the shape functions to link the membrane strains with the nodal displacements which are given in Appendix.

After assembling the above single element equation to the global matrix system and applying the boundary conditions, the nodal displacements of the structure can be estimated. After obtaining the displacement field, the stress intensity factor (SIF) can be calculated by the Displacement Extrapolation Method (Zhu and Oterkus, 2020). For plane elements, only two types of SIF can occur, which are opening SIF

**Table 3**
The results of Case 2.

| Case 2 | | $U$ (m) | $V$ (m) | SIF-$K_I$ |
|---|---|---|---|---|
| (a) | FEM | 6.589E-03 | 4.154E-02 | 2.089E+09 |
| (b) | iFEM | 6.466E-03 | 4.222E-02 | 1.924E+09 |
| Differences between (a) and (b) | | 1.87% | 1.64% | 7.91% |

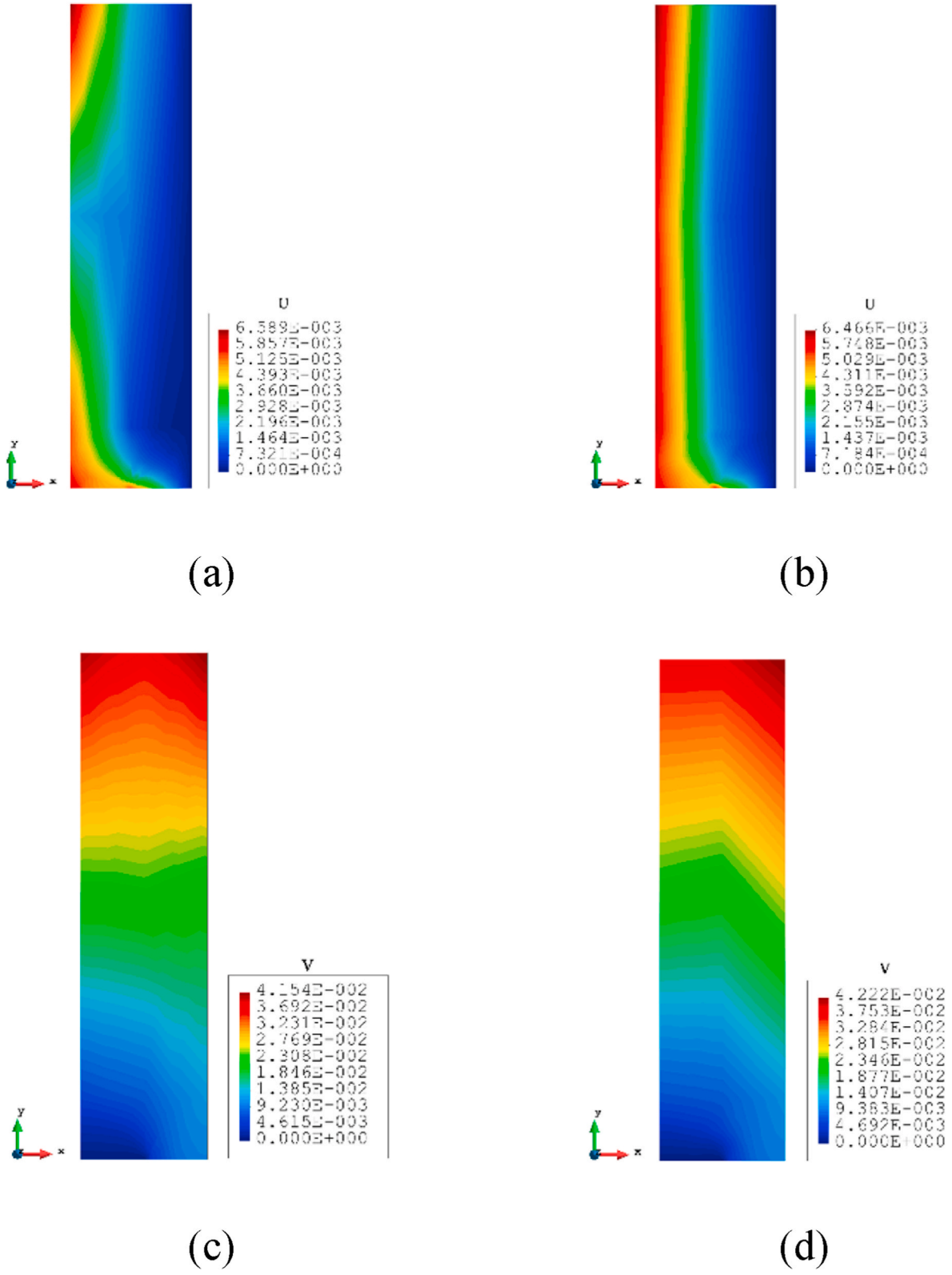


**Fig. 8.** The contour plots for Case 2. The displacements in x-direction, $U$: (a) FEM, (b) iFEM. The displacements in y-direction, $V$: (c) FEM, (d) iFEM.

($K_I$) and in-plane shear SIF ($K_{II}$). Fig. 2 shows the nodes around the crack tip ($r = 0$). For the nodes at the crack surface ($\theta = 180°$), the relationship between the SIF and the nodal displacements can be expressed (Zhu and Oterkus, 2020):

$$K_I = \sqrt{2\pi}\,\frac{G}{1+k_b}\,\frac{|\Delta V|}{\sqrt{r}} \tag{6a}$$

$$K_{II} = \sqrt{2\pi}\,\frac{G}{1+k_b}\,\frac{|\Delta U|}{\sqrt{r}} \tag{6b}$$

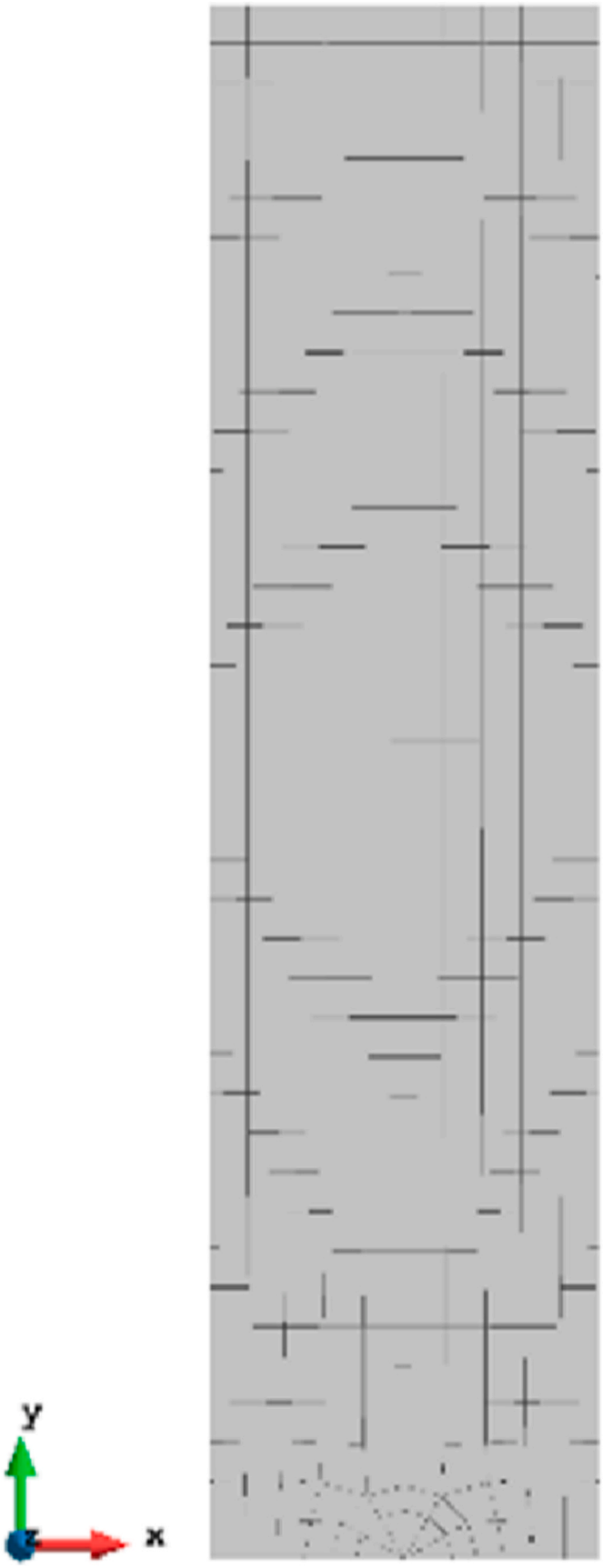


**Fig. 9.** Mesh for Case 3 (edge crack) and Case 4 (central crack).

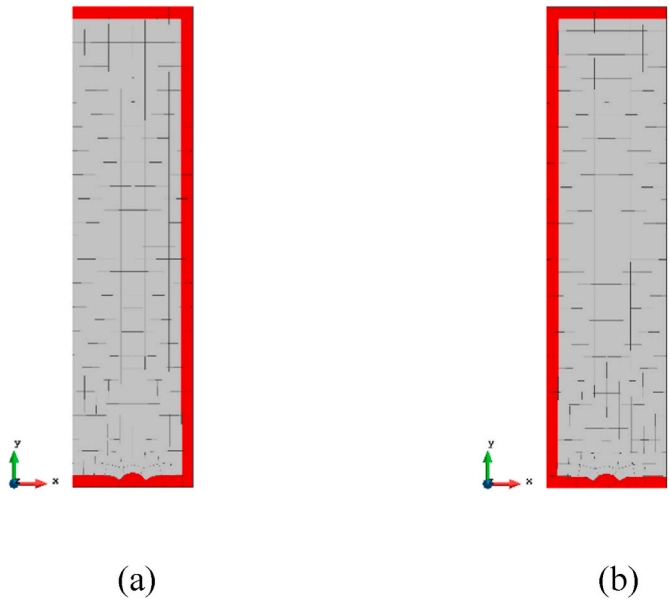


**Fig. 10.** The sensor locations for (a) Case 3 and (b) Case 4.

**Table 4**
The results for Case 3.

| Case 3 | | $U$ (m) | $V$ (m) | SIF-$K_I$ |
|---|---|---|---|---|
| (a) | FEM | 5.056E-03 | 4.097E-02 | 2.077E+09 |
| (b) | iFEM | 4.596E-03 | 4.072E-02 | 2.001E+09 |
| (c) | iFEM-r | 4.775E-03 | 3.983E-02 | 2.012E+09 |
| Differences between (a) and (b) | | 9.10% | 0.61% | 3.66% |
| Differences between (a) and (c) | | 5.56% | 2.78% | 3.12% |

$G$ is the shear modulus, and it can be calculated by the Elastic modulus, $E$, and the Poisson's ratio, $\nu$. $k_b$ is the bulk modulus, and under the plane strain conditions, $k_b = 3 - 4\nu$, and under the plane stress conditions, $k_b = \frac{3-\nu}{1+\nu}$. $|\Delta V|$ and $|\Delta U|$ are the relative displacements in y- and x-directions for the nodes next to the crack tip. If the structure is modelled fully (Fig. 2(a)), $|\Delta V_{im}| = |V_i - V_m|$ and $|\Delta U_{im}| = |U_i - U_m|$. Otherwise, for the half model (see Fig. 2(b)), $|\Delta V| = |2V_i|$ and $|\Delta U| = |2U_i|$.

$\frac{|\Delta V|}{\sqrt{r}}$ and $\frac{|\Delta U|}{\sqrt{r}}$ are assumed to be linear at the crack surface and they can be obtained by approaching $r$ to 0 for the crack tip as:

$$\text{For} K_I : \frac{|\Delta V|}{\sqrt{r}} = \frac{|\Delta V_{im}|(d_2)^{\frac{3}{2}} - |\Delta V_{jn}|(d_1)^{\frac{3}{2}}}{\sqrt{d_1 d_2}(d_2 - d_1)} \tag{7a}$$

$$\text{For} K_{II} : \frac{|\Delta U|}{\sqrt{r}} = \frac{|\Delta U_{im}|(d_2)^{\frac{3}{2}} - |\Delta U_{jn}|(d_1)^{\frac{3}{2}}}{\sqrt{d_1 d_2}(d_2 - d_1)} \tag{7b}$$

where $d_1$ is the distance between $k$ and $i$ ($k$ and $m$) and $d_2$ is the distance between $k$ and $j$ ($k$ and $n$).

## 3. Numerical examples

As shown in Table 1, six numerical cases are considered to test the accuracy of the inverse crack tip element and demonstrate its capability in estimating the SIF. For all six cases, elastic modulus, $E$, is $210 \times 10^9$ Pa and Poisson's ratio, $\nu$, is 0.3.

The initial four cases are prepared to compare with the reference results and investigate the effect of mesh size on the accuracy of the results for the opening mode. For Case 5 and Case 6, in-plane shear and mixed-mode SIF estimation are given to show the capability of the iPCT element. An in-house code written by using Matlab programming

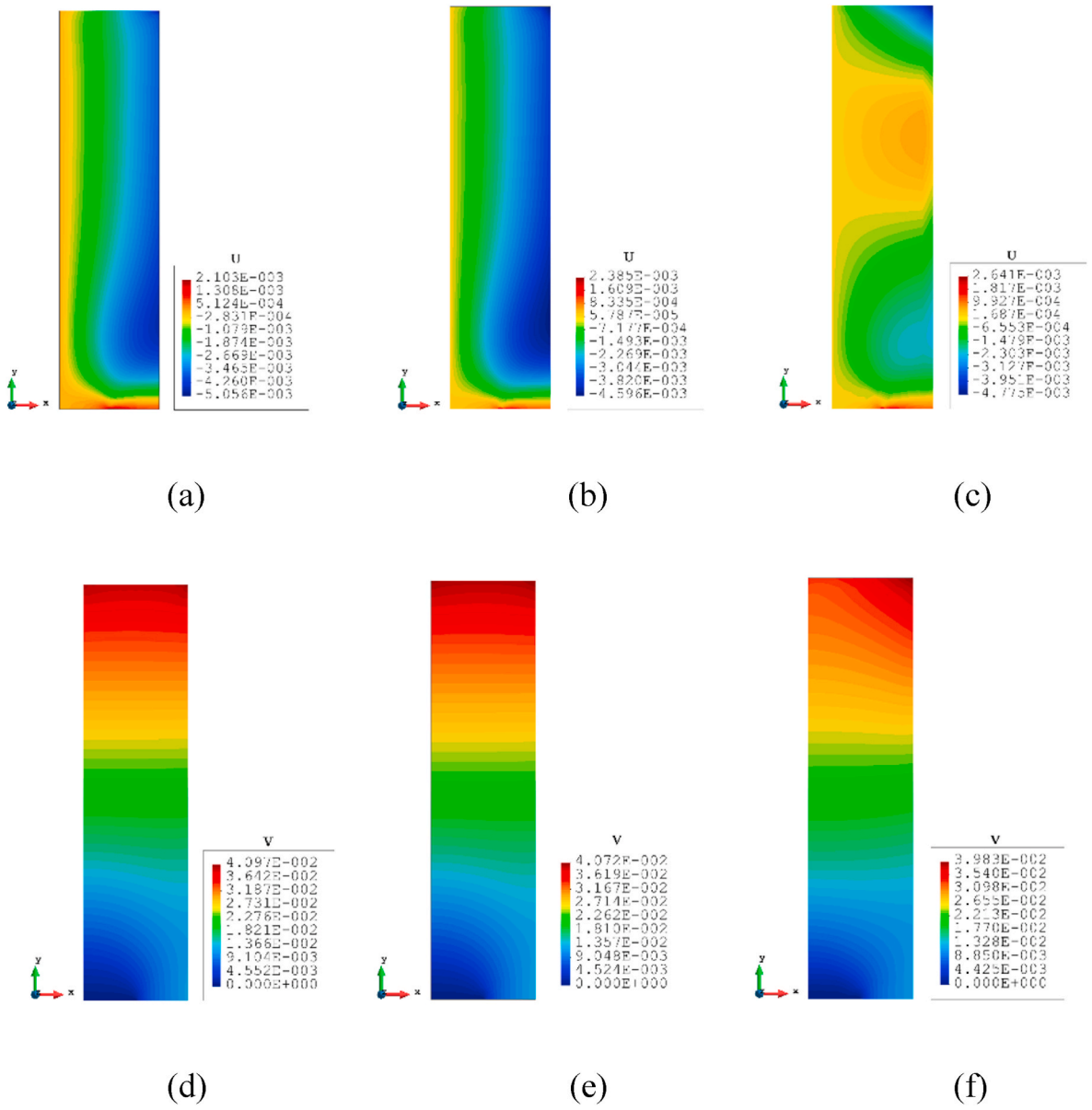


**Fig. 11.** The plots for Case 3. The displacements in x-direction, $U$: (a) FEM, (b) iFEM, (c) iFEM-r. The displacements in y-direction, $V$: (d) FEM, (e) iFEM, (f) iFEM-r.

**Table 5**
The results of Case 4.

| Case 4 | | $U$ (m) | $V$ (m) | SIF-$K_I$ |
|---|---|---|---|---|
| (a) | FEM | 5.805E-03 | 4.067E-02 | 2.113E+09 |
| (b) | iFEM | 5.853E-03 | 4.041E-02 | 2.045E+09 |
| (c) | iFEM-r | 5.478E-03 | 4.005E-02 | 2.090E+09 |
| Differences between (a) and (b) | | 0.83% | 0.64% | 3.25% |
| Differences between (a) and (c) | | 5.63% | 1.52% | 1.13% |

language was developed for computer implementation of the present approach. A flow chart of the analysis process is given in Fig. 3.

### 3.1. Case 1: rectangular bar with two edge cracks

The first case is a rectangular bar with two edge cracks under plane strain conditions. The geometry of the plate is shown in Fig. 4(a). Since the plate is under tension (2000 MN and evenly distributed to the nodes) on the top and bottom edges, symmetry boundary conditions can be applied (see Fig. 4(b)). Therefore, only a quarter of the plate is modelled. For Case 1, a very coarse mesh, which has only 20 elements and 65 nodes, is generated for the reference FEM analysis (see Fig. 5(a)). For the iFEM analysis, to avoid the general triangular elements, the mesh has been refined with entire quadrilateral elements (still 20 elements but with 69 nodes) except the 6 inverse crack tip elements around the crack tip (Fig. 5(b)). The results of Case 1 are collected in Table 2 and the contour plots of deformations are given in Fig. 6.

By comparing major displacements, both $U$ and $V$ are in good agreement with FEM results and the percentages of the difference are smaller than 5%. Moreover, the contour plots of the iFEM are also similar to the FEM plots. The inverse crack tip elements combined with the inverse 8-node plane quadrilateral elements can provide accurate displacement results. For SIF, FEM provides a value of $2.017 \times 10^9$, and iFEM has slightly under-estimated the value and achieves a value of $1.870 \times 10^9$, leading to a 7.31% error which is still in a reasonable range, proving that the inverse crack tip element can be used to monitor the SIF data.

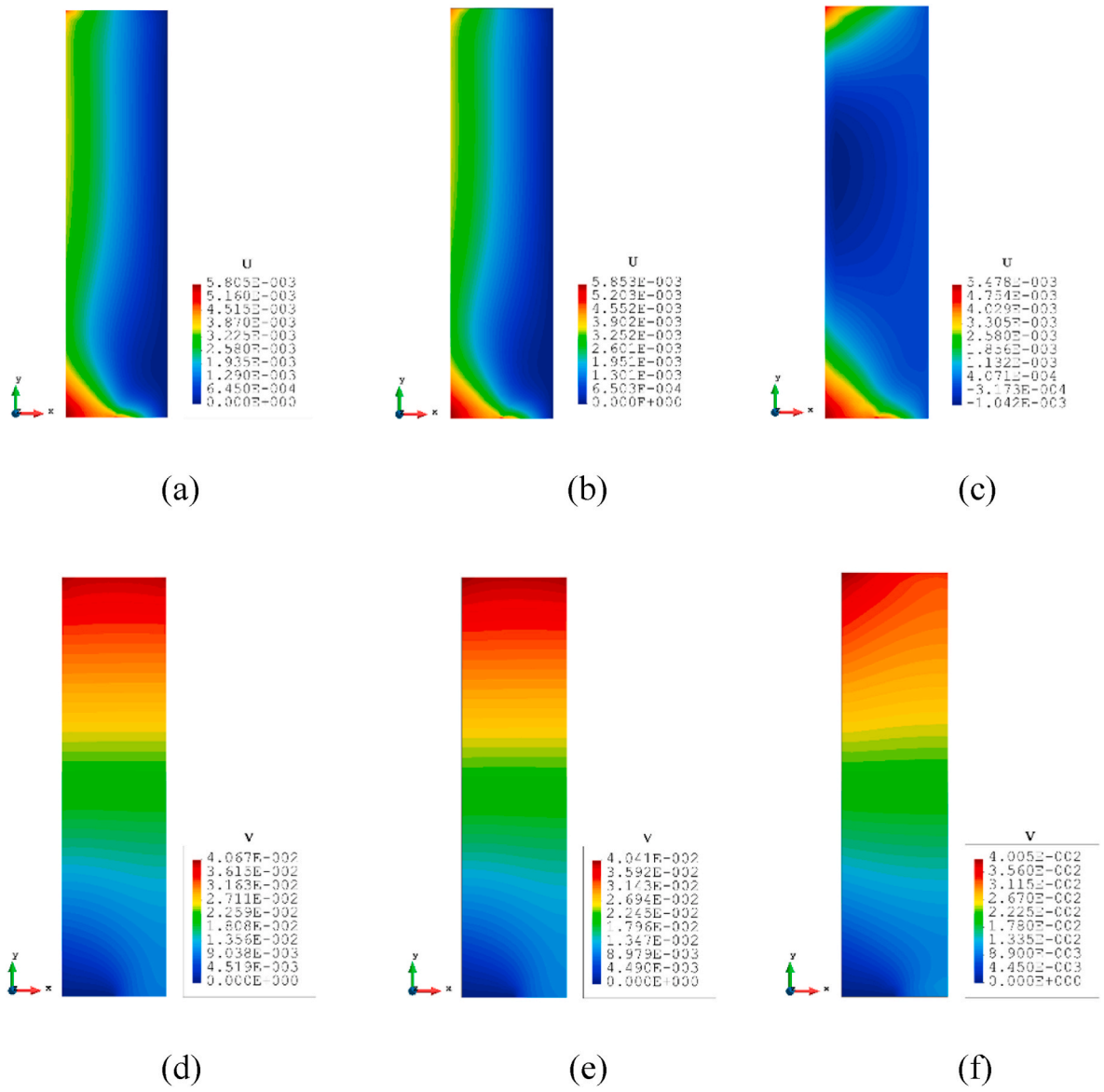


**Fig. 12.** The contour plots for Case 4. The displacements in x-direction, *U*: (a) FEM, (b) iFEM, (c) iFEM-r. The displacements in y-direction, *V*: (d) FEM, (e) iFEM, (f) iFEM-r.

### 3.2. Case 2: rectangular bar with a central crack

For the second case, rectangular bar with a central crack problem is considered as shown in Fig. 7(a). As opposed to previous case, the constrained boundary condition on the right edge is moved to the left edge making it become a quarter of the model with a central crack (see Fig. 7(b)). Other parameters including the length of the crack keep unchanged. As can be seen from Table 3 and Fig. 8, the results including the contour plots match well with FEM analysis. The percentage of the difference between the two SIF values is about 7%. Although this is a reasonable difference, the difference between iFEM and FEM results can be further reduced by increasing the number of sensors especially around the crack tip region.

### 3.3. Case 3: fine mesh for the rectangular bar with two edge crack case

Increasing the number of elements for the iFEM analysis can improve accuracy. Case 3 and Case 4 are the fine mesh condition for Case 1 and Case 2, respectively, and there are 408 elements and 1321 nodes in the model (Fig. 9). For the fine mesh cases, the reduced-sensor condition is also considered to test the feasibility of the inverse crack tip element with limited number of strain inputs (iFEM-r). For Cases 3 and 4, 64 sensors can be sufficient by collecting strain data from elements with red colour shown in Fig. 10(a) and (b).

For Case 3, according to Table 4, it can be seen that both full-sensor and reduced-sensor conditions can give accurate displacements in the y-direction. But for *U* displacement, the percentages of the difference raise especially for the full-sensor condition, which is 9.10%. Please note that compared with the major displacements, *V*, the maximum *U* displacement is about 8 times smaller. Because of this reason, the displacements in the x-direction will not have a big impact on the SIF calculation. Hence, about 10% is still acceptable. The SIF from the full-sensor condition is only 3.66% less than the reference value and for the iFEM analysis with 64 sensors (iFEM-r), the value (3.12%) is even better than the full-sensor case. Concerning the contour plots of Case 3 (Fig. 11), the plots of the full-sensor condition are almost the same as the FEM plots. For the reduced-sensor condition, due to the reduction of sensors, some regions suffer loss of accuracy, especially for the plots of *U*. However, the main features like the locations of the large deformations can still be captured.

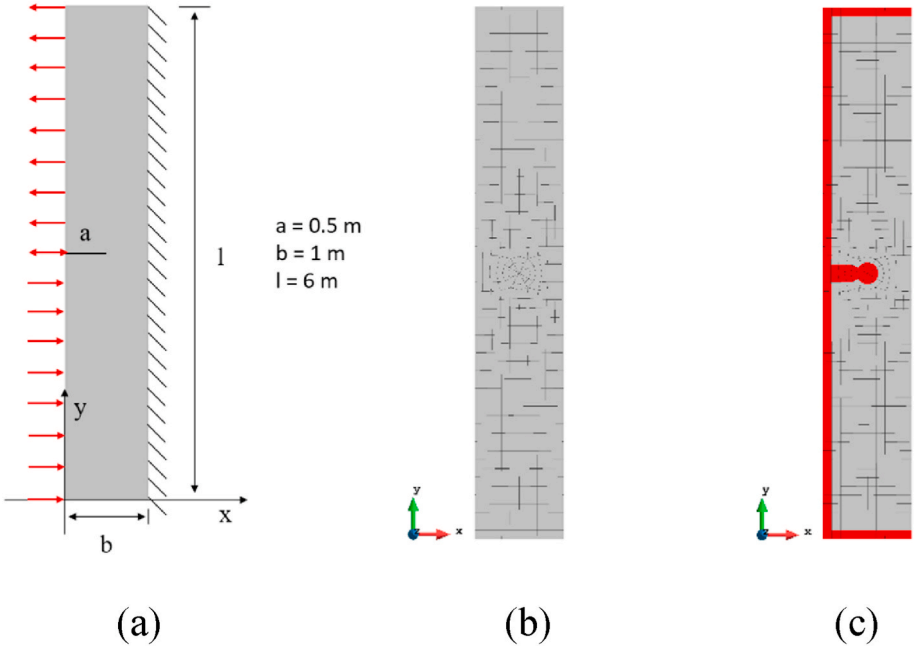


**Fig. 13.** (a) The geometry, loading, and boundary conditions for Case 5. (b) The mesh of both FEM and iFEM analysis for Case 5. (c) The sensor locations for Case 5 for reduced-sensor condition.

**Table 6**
The results of Case 5.

| Case 5 | | $U$ (m) | $V$ (m) | SIF- $K_{II}$ |
|---|---|---|---|---|
| (a) | FEM | 1.310E-04 | 6.126E-04 | 1.259E+07 |
| (b) | iFEM | 1.246E-04 | 5.576E-04 | 1.287E+07 |
| (c) | iFEM-r | 1.247E-04 | 5.512E-04 | 1.276E+07 |
| Differences between (a) and (b) | | 4.89% | 8.98% | 2.15% |
| Differences between (a) and (c) | | 4.81% | 10.02% | 1.35% |

### 3.4. Case 4: fine mesh for the rectangular bar with a central crack case

When it comes to the central crack case, the performance of the full-sensor condition becomes much better. All values (Table 5) together with the contour plots (Fig. 12) are highly close to the FEM results. When the number of sensors is dropped to 64 (iFEM-r), although the vertical displacement, $V$, is 5.63% less than the reference value, the other results, especially the desired SIF, are approximately the same as the FEM analysis. For the contour plots, they demonstrate similar trend as Case 3 and some regions do not have the same accuracy as full-sensor plots. Considering the less importance of these regions and achieving sufficient reduction in number of sensors, current sensor locations can be applicable and even with a limited number of sensors, not only the deformations but also the SIF can be captured accurately.

### 3.5. Case 5: in-plane shear SIF case

The previous four cases focus on the opening SIF. So, the following case will be related to the pure in-plane shear SIF condition. $K_{\mathrm{I}}$ still exists because of the Poisson's ratio, but it is quite small and can be neglected.

The geometry of the model is slightly updated (see Fig. 13) and the plane strain condition is changed to plane stress. Besides, because of change in loading (1000 KN for each node) and the boundary condition (fully constrained at the right edge), the symmetrical boundary condition can no longer be used. Therefore, the whole plate is modelled and meshed with 616 elements and 1989 nodes. Around the crack tip, there are 12 finite/inverse crack tip elements. For the reduced-sensor condition (iFEM-r), 98 elements are selected to provide strain data and these sensors can be categorized into three groups: the boundary sensors, the crack tip sensors, and the connection sensors to join the previous two types together. It should be highlighted that for the crack tip, it is recommended that all 12 sensors should be chosen, otherwise, the accuracy of the SIF will be negatively influenced. For Case 5, the displacements in the x-direction become the major displacement and the in-plane shear SIF can be computed by Eq. (7b). Table 6 shows the errors of the major displacements that are less than 5% for both sensor conditions.

Although the displacements in the y-direction are less for Case 5, the values are still in the acceptable range. The in-plane shear SIFs are slightly higher than the reference value, which fulfils the aim of the analysis. The contour plots of Fig. 14 can support the above standpoints, and the main features and tendency of the iFEM deformation field are identical to the FEM plots, apart from some regions in the plots of the reduced-sensor condition which are less accurate. The accuracy level in the reduced-sensor case can be improved by increasing the number of sensors.

### 3.6. Case 6: mixed-mode SIF case

The last case is generated based on Case 5 (see Fig. 15). The main difference is replacing the distributed forces on the left edge with two nodal forces at the upper right corner in both positive axes and forces have same values. Besides, the fully constrained boundary condition has been moved to the bottom of the plate. As a result of the relatively more complex loading and boundary conditions, the number of sensors increases to 156 by adding the boundary sensors along the right edge.

The results of Case 6 are listed in Table 7. Even though the maximum $V$ displacement is about 5.69% higher than the reference one, the errors of the displacements are held to a reasonable extent. For the SIF, since the in-plane shear SIF is relatively smaller than the opening SIF, it is expected that the error for $K_{II}$ may be higher than the error for $K_{\mathrm{I}}$. For the full-sensor condition, the gap between the two errors is not far away from each other. For the in-plane shear SIF, the error value is 5.40% which is even better than the opening SIF (7.76%). However, for the 156 sensors case (reduced-sensor condition, iFEM-r), the percentage error for the opening SIF is more than two times smaller than the percentage error for in-plane shear SIF. However, 10.61% is still within acceptable range. Please note that $K_{\mathrm{I}}$ is about 20 times larger than $K_{II}$. The contour

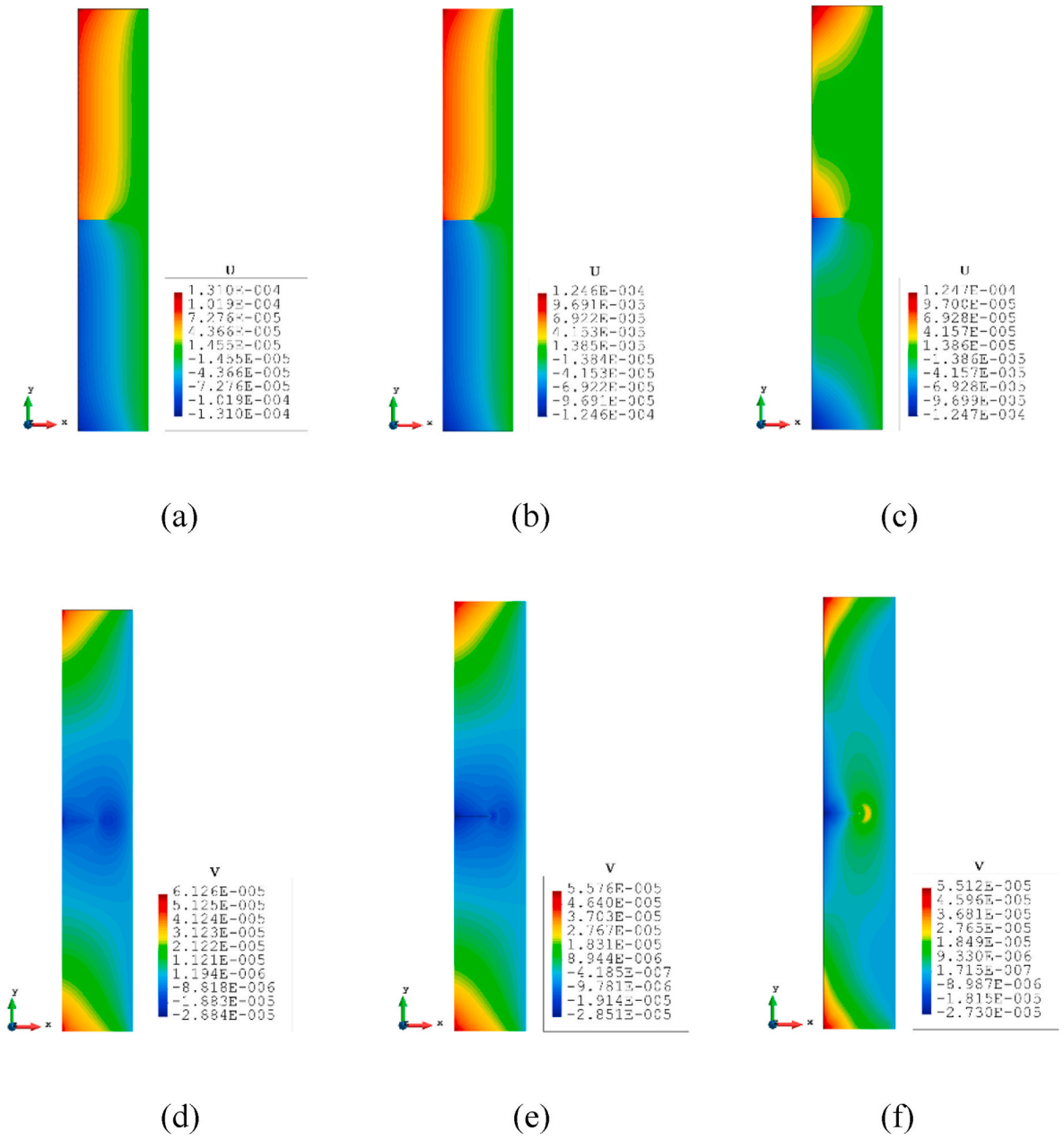


**Fig. 14.** The plots for Case 5. The displacements in x-direction, *U*: (a) FEM, (b) iFEM, (c) iFEM-r. The displacements in y-direction, *V*: (d) FEM, (e) iFEM, (f) iFEM-r.

plots of iFEM analysis for both with full sensors and reduced sensors are not distinguishable against the FEM reference solution, which also supports the above conclusions (see Fig. 16). Case 5 and Case 6 present that for different modes of SIF, the inverse crack tip element can estimate the SIF value with high accuracy.

## 4. Conclusions

In this study, a new two-dimensional inverse crack tip element was presented for shape sensing and structural health monitoring purposes. Based on the six numerical cases, it can be concluded that the newly developed inverse crack tip element can increase the capability of the iFEM methodology by not only predicting the full-field deformation but also eliminating the limitation of iFEM when dealing with structures with cracks and monitoring the SIF around the crack tip. If the strain data for the inverse crack tip elements are all available, even if the number of sensors for the other regions are reduced, SIF values together with the displacements can still be accurately predicted.

The developed iPCT element can accurately represent the deformation and stress fields, including stress singularity, around the crack tip which cannot be easily done by using traditional elements without utilising large number of elements. Therefore, the required number of sensors can be significantly reduced. By accurately determining the SIF values at the crack tip can allow crack propagation predictions by using suitable failure criteria. The developed approach can be utilised in many applications which cracks can occur such as aerospace, marine, and civil engineering applications.

## CRediT authorship contribution statement

**Mingyang Li:** Conceptualization, Methodology, Software, Writing – original draft. **Erkan Oterkus:** Conceptualization, Methodology, Supervision, Writing – review & editing. **Selda Oterkus:** Conceptualization, Methodology, Supervision, Writing – review & editing.

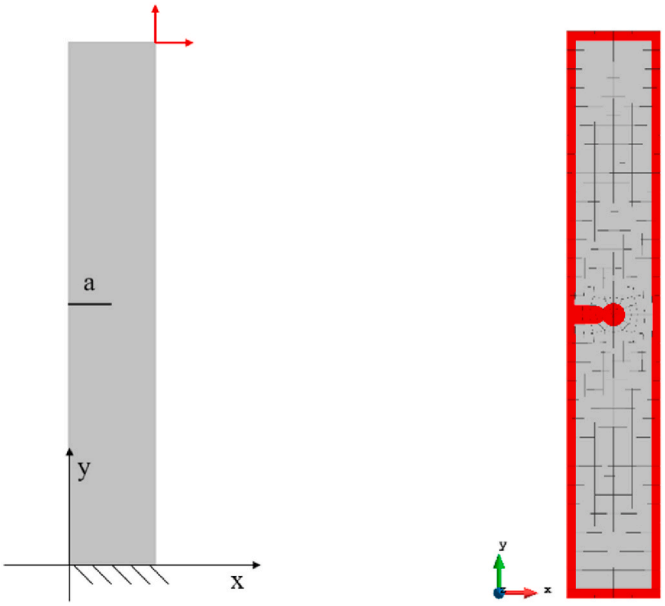


**Fig. 15.** (a) The geometry, loading, and boundary conditions for Case 6. (b) Mesh and the sensor locations for Case 6 for reduced-sensor condition.

**Table 7**
The results of Case 6.

| Case 6 | | $U$ (m) | $V$ (m) | SIF-$K_I$ | SIF-$K_{II}$ |
|---|---|---|---|---|---|
| (a) | FEM | 5.357E-03 | 8.839E-04 | 3.181E+07 | 1.691E+06 |
| (b) | iFEM | 5.501E-03 | 9.342E-04 | 3.428E+07 | 1.600E+06 |
| (c) | iFEM-r | 5.159E-03 | 8.612E-04 | 3.045E+07 | 1.512E+06 |
| Differences between (a) and (b) | | 2.68% | 5.69% | 7.76% | 5.40% |
| Differences between (a) and (c) | | 3.70% | 2.57% | 4.29% | 10.61% |

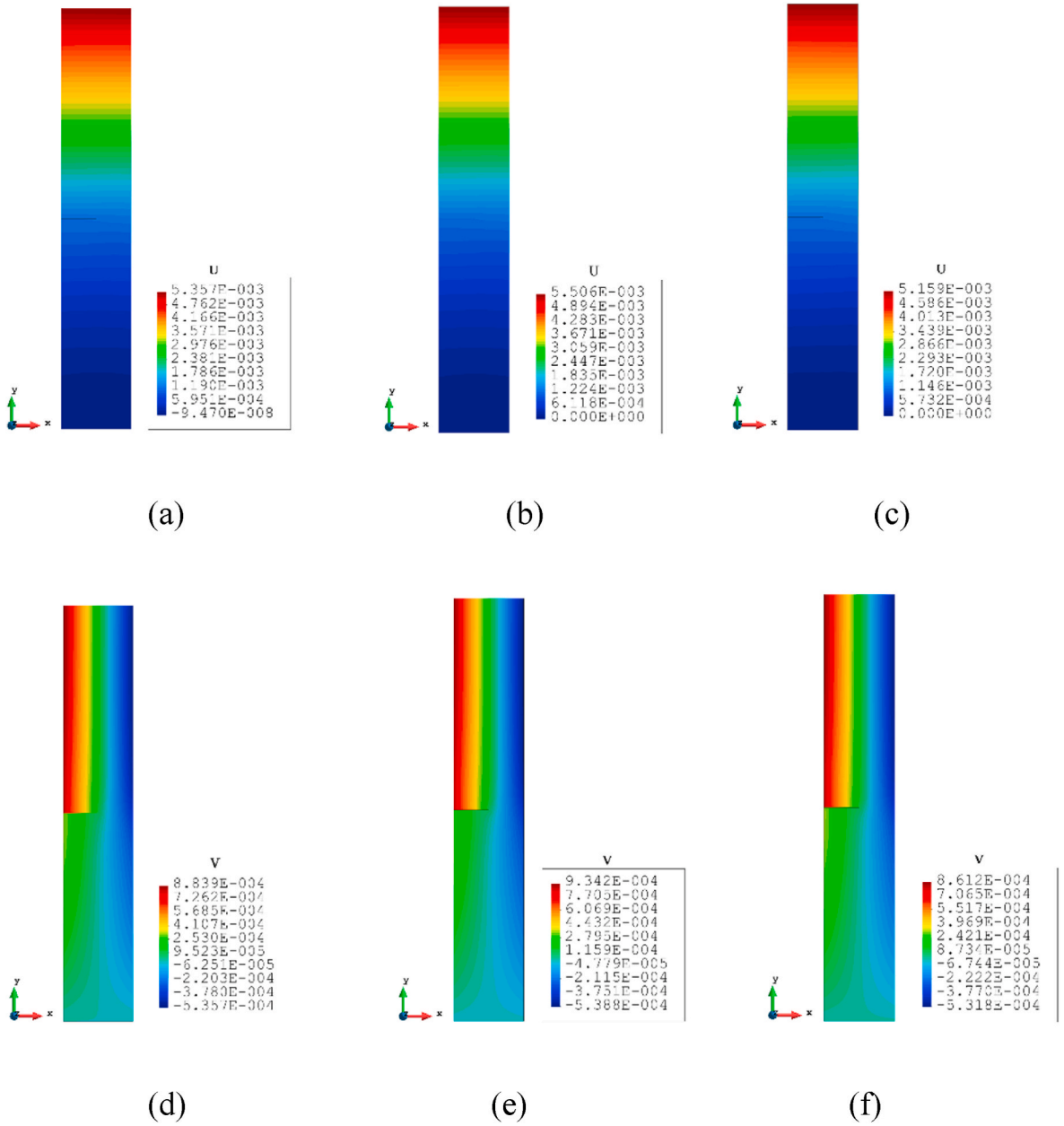


**Fig. 16.** The plots for Case 6. The displacements in x-direction, $U$: (a) FEM, (b) iFEM, (c) iFEM-r. The displacements in y-direction, $V$: (d) FEM, (e) iFEM, (f) iFEM-r.

## Declaration of competing interest

The authors declare that they have no known competing financial interests or personal relationships that could have appeared to influence the work reported in this paper.

## Data availability

Data will be made available on request.

## Appendix

In this section, the details of the $\mathbf{B}^m$ matrix included in Eq. (5a,b) is given. $\mathbf{B}^m$ is the matrix formed by the shape functions of each node for a two-dimensional eight-node quadrilateral inverse element (see Fig. A1(a)) as $\mathbf{B}^m = [\,\mathbf{B}_1^m \quad \mathbf{B}_2^m \quad \mathbf{B}_3^m \quad \mathbf{B}_4^m \quad \mathbf{B}_5^m \quad \mathbf{B}_6^m \quad \mathbf{B}_7^m \quad \mathbf{B}_8^m\,]^T$. The master element has a square shape and defined in the natural coordinate system $(\xi, \eta)$ as depicted in Fig. A1(b).

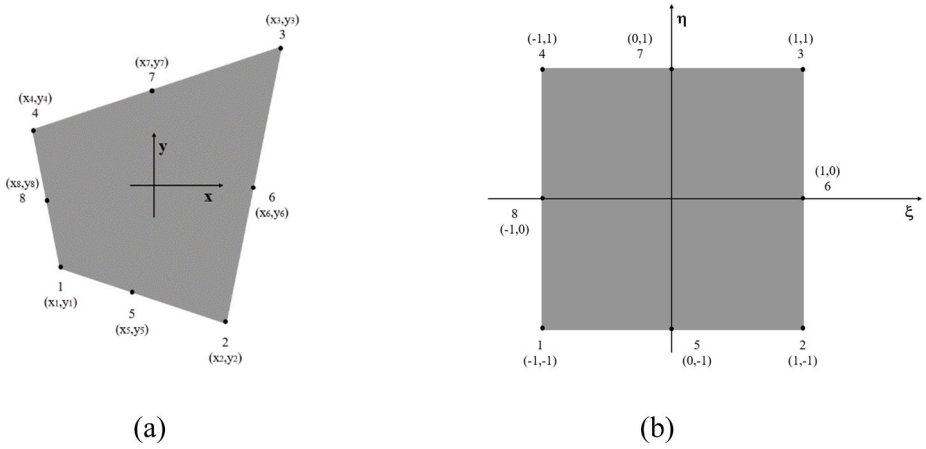


**Fig. A1.** **(a)** Two-dimensional eight-node quadrilateral inverse element, **(b)** the master element in $(\xi, \eta)$ space.

Every single $\mathbf{B}_i^m$ matrix can be defined as

$$\mathbf{B}_i^m = \begin{bmatrix} \dfrac{\partial N_i}{\partial x} & 0 \\ 0 & \dfrac{\partial N_i}{\partial y} \\ \dfrac{\partial N_i}{\partial y} & \dfrac{\partial N_i}{\partial x} \end{bmatrix} \tag{A1}$$

where the bilinear isoparameteric shape functions, $N_i(\xi, \eta)$, are defined as

$$N_1 = \frac{(1-\xi)(1-\eta)(-1-\xi-\eta)}{4} \tag{A2a}$$

$$N_2 = \frac{(1+\xi)(1-\eta)(-1+\xi-\eta)}{4} \tag{A2b}$$

$$N_3 = \frac{(1+\xi)(1+\eta)(-1+\xi+\eta)}{4} \tag{A2c}$$

$$N_4 = \frac{(1-\xi)(1+\eta)(-1-\xi-\eta)}{4} \tag{A2d}$$

$$N_5 = \frac{(1-\xi)(1+\xi)(1-\eta)}{2} \tag{A2e}$$

$$N_6 = \frac{(1+\xi)(1+\eta)(1-\eta)}{2} \tag{A2f}$$

$$N_7 = \frac{(1-\xi)(1+\xi)(1+\eta)}{2} \tag{A2g}$$

$$N_8 = \frac{(1-\xi)(1+\eta)(1-\eta)}{2} \tag{A2h}$$

## References


Bang, H.J., Kim, H.I., Lee, K.S., 2012. Measurement of strain and bending deflection of a wind turbine tower using arrayed FBG sensors. Int. J. Precis. Eng. Manuf. 13 (12), 2121–2126.

Barsoum, R.S., 1976. On the use of isoparametric finite elements in linear fracture mechanics. Int. J. Numer. Methods Eng. 10 (1), 25–37.

Barsoum, R.S., 1977. Triangular quarter-point element as elastic and perfectly-plastic crack tip elements. int. J. numer. Merh. Engng 11 (85), 98.

Cerracchio, P., Gherlone, M., Di Sciuva, M., Tessler, A., 2015. A novel approach for displacement and stress monitoring of sandwich structures based on the inverse Finite Element Method. Compos. Struct. 127, 69–76.

Chen, L., Choy, Y.S., Wang, T.G., Chiang, Y.K., 2020. Fault detection of wheel in wheel/rail system using kurtosis beamforming method. Struct. Health Monit. 19 (2), 495–509.

Colombo, L., Sbarufatti, C., Giglio, M., 2019. Definition of a load adaptive baseline by inverse finite element method for structural damage identification. Mech. Syst. Signal Process. 120, 584–607.

De Mooij, C., Martinez, M., Benedictus, R., 2019. iFEM benchmark problems for solid elements. Smart Mater. Struct. 28 (6), 065003.

Di Sante, R., 2015. Fibre optic sensors for structural health monitoring of aircraft composite structures: recent advances and applications. Sensors 15 (8), 18666–18713.

Gherlone, M., Cerracchio, P., Mattone, M., Di Sciuva, M., Tessler, A., 2012. Shape sensing of 3D frame structures using an inverse finite element method. Int. J. Solid Struct. 49 (22), 3100–3112.

Kefal, A., 2019. An efficient curved inverse-shell element for shape sensing and structural health monitoring of cylindrical marine structures. Ocean Eng. 188, 106262.

Kefal, A., Oterkus, E., 2015. Structural Health Monitoring of Marine Structures by Using Inverse Finite Element Method. *Analysis And Design Of Marine Structures V*, pp. 341–349.

Kefal, A., Oterkus, E., 2016a. Displacement and stress monitoring of a chemical tanker based on inverse finite element method. Ocean Eng. 112, 33–46.

Kefal, A., Oterkus, E., 2016b. Displacement and stress monitoring of a Panamax containership using inverse finite element method. Ocean Eng. 119, 16–29.

Kefal, A., Oterkus, E., 2020. Isogeometric iFEM analysis of thin shell structures. Sensors 20 (9), 2685.

Kefal, A., Oterkus, E., Tessler, A., Spangler, J.L., 2016. A quadrilateral inverse-shell element with drilling degrees of freedom for shape sensing and structural health monitoring. Engineering science and technology, an international journal 19 (3), 1299–1313.

Kefal, A., Mayang, J.B., Oterkus, E., Yildiz, M., 2018a. Three dimensional shape and stress monitoring of bulk carriers based on iFEM methodology. Ocean Eng. 147, 256–267.

Kefal, A., Tessler, A., Oterkus, E., 2018b. An Efficient Inverse Finite Element Method for Shape and Stress Sensing of Laminated Composite and Sandwich Plates and Shells. NASA/TP-2018-220079 (No. L-20938).

Kinet, D., Mégret, P., Goossen, K.W., Qiu, L., Heider, D., Caucheteur, C., 2014. Fiber Bragg grating sensors toward structural health monitoring in composite materials: challenges and solutions. Sensors 14 (4), 7394–7419.

Ko, W.L., Richards, W.L., Tran, V.T., 2007. Displacement Theories for In-Flight Deformed Shape Predictions of Aerospace Structures. No. H-2652).

Kromanis, R., Kripakaran, P., 2016. SHM of bridges: characterising thermal response and detecting anomaly events using a temperature-based measurement interpretation approach. Journal of Civil Structural Health Monitoring 6, 237–254.

Li, M., Dirik, Y., Oterkus, E., Oterkus, S., 2023. Shape sensing of NREL 5 MW offshore wind turbine blade using iFEM methodology. Ocean Eng. 273, 114036.

Lu, B., Li, Y., Wu, X., Yang, Z., 2009. A review of recent advances in wind turbine condition monitoring and fault diagnosis. In: 2009 IEEE Power Electronics and Machines in Wind Applications, pp. 1–7. IEEE.

Nikishkov, G.P., 2013. Accuracy of quarter-point element in modeling crack-tip fields. CMES Comp Model Eng 93 (5), 335–361.

Tessler, A., Spangler, J.L., 2003. A Variational Principle for Reconstruction of Elastic Deformations in Shear Deformable Plates and Shells. NASA/TM-2003-212445.

Tessler, A., Spangler, J.L., 2004. Inverse FEM for full-field reconstruction of elastic deformations in shear deformable plates and shells. In: 2nd European Workshop on Structural Health Monitoring, pp. 7–9. July 2004, Munich, Germany.

Tessler, A., Spangler, J.L., Gherlone, M., Mattone, M., Di Sciuva, M., 2012. Deformed shape and stress reconstruction in plate and shell structures undergoing large displacements: application of inverse finite element method using fiber bragg grating strains. In: Proceedings of 10th World Congress on Computational Mechanics. Sao Paulo, Brazil.

Xiong, R., Li, L., Tian, J., 2018. Towards a smarter battery management system: a critical review on battery state of health monitoring methods. J. Power Sources 405, 18–29.

Zhao, F., Bao, H., 2021. An improved inverse finite element method for shape sensing using isogeometric analysis. Measurement 167, 108282.

Zhao, F., Xu, L., Bao, H., Du, J., 2020. Shape sensing of variable cross-section beam using the inverse finite element method and isogeometric analysis. Measurement 158, 107656.

Zhu, N., Oterkus, E., 2020. Calculation of stress intensity factor using displacement extrapolation method in peridynamic framework. Journal of Mechanics 36 (2), 235–243.